Journal of Computational Physics 372 (2018) 823–840

Contents lists available at ScienceDirect

Journal of Computational Physics

www.elsevier.com/locate/jcp

A phase-field model for fluid–structure interaction

Dominic Mokbel [a], Helmut Abels [b], Sebastian Aland [a,c,*]

[a] Institut für wissenschaftliches Rechnen, Technische Universität Dresden, 01062 Dresden, Germany
[b] Fakultät für Mathematik, Universität Regensburg, 93040 Regensburg, Germany
[c] Fakultät Informatik/Mathematik, Hochschule für Technik und Wirtschaft Dresden, 01069 Dresden, Germany

ARTICLE INFO

Article history:
Received 7 March 2018
Received in revised form 1 June 2018
Accepted 23 June 2018
Available online 28 June 2018

Keywords:
Fluid–structure interaction
Phase-field
Diffuse interface
Viscoelasticity
Contact problem
Fully Eulerian

ABSTRACT

In this paper, we develop a novel phase-field model for fluid–structure interaction (FSI), that is capable to handle very large deformations as well as topology changes like contact of the solid to a wall. The model is based on a fully Eulerian description of the velocity field in both, the fluid and the elastic domain. Viscous and elastic stresses in the Navier–Stokes equations are restricted to the corresponding domains by multiplication with their characteristic functions. The solid is described as a hyperelastic neo-Hookean material and the elastic stress is obtained by solving an additional Oldroyd-B – like equation. Thermodynamically consistent forces are derived by energy variation. The convergence of the derived equations to the traditional sharp interface formulation of fluid–structure interaction is shown by matched asymptotic analysis. The model is evaluated in a challenging benchmark scenario of an elastic body traversing a fluid channel. A comparison to reference values from Arbitrary Lagrangian Eulerian (ALE) simulations shows very good agreement. We highlight some distinct advantages of the new model, like the avoidance of re-triangulations and the stable inclusion of surface tension. Further, we demonstrate how simple it is to include contact dynamics into the model, by simulating a ball bouncing off a wall. We extend this scenario to include adhesion of the ball, which to our knowledge, cannot be simulated with any other FSI model. While we have restricted simulations to fluid–structure interaction, the model is capable to simulate any combination of viscous fluids, visco-elastic fluids and elastic solids.

1. Introduction

In fluid–structure interaction (FSI) problems, a solid structure interacts with an internal or surrounding fluid. Such problems arise in many scientific and engineering applications, for example in aeroelasticity, sedimentation, biological fluids and biomechanics, see [18] for a recent review. Yet the modeling of FSI problems is mathematically challenging due to the fundamental differences of the involved materials: a continually deforming (i.e. flowing) fluid, as opposed to a structurally rigid solid whose atoms are tightly bound to each other.

Most modeling approaches deal with this discrepancy by introducing two different coordinate systems and two numerical meshes for the two materials. The most popular approach is the Arbitrary Lagrangian–Eulerian (ALE) method [19] in which the computational domain is subdivided into a fluid domain Ω_f and a structure domain Ω_s. The elastic structure is described in the Lagrangian coordinate system, with deformations captured in a displacement vector field. On the con-

* Corresponding author.
E-mail addresses: dominic.mokbel@tu-dresden.de (D. Mokbel), helmut.abels@mathematik.uni-regensburg.de (H. Abels), sebastian.aland@htw-dresden.de (S. Aland).

https://doi.org/10.1016/j.jcp.2018.06.063
0021-9991/

trary, the fluid domain is described in an Eulerian coordinate system and the variable of interest is the velocity field. Both meshes are aligned at the fluid/solid interface which is typically moved with the calculated velocity. While this methodology provides a sound mathematical description and leads to a very accurate domain representation, it also comes with limitations on the evolution of the solid structure, which breaks down for large deformations or large translational and rotational movements. Hence, even simple scenarios like an elastic body moving through a viscous fluid may become impossible to simulate, since technically advanced (re-)triangulation methods and clever interpolations are needed. This has led to the development of alternative modeling approaches in recent years, in particular fully Eulerian formulations [13] and interface capturing methods.

In interface capturing methods, the fluid and solid domain and their respective interface are implicitly described by an additional field variable. Most popular interface capturing methods are the level-set [27], volume-of-fluid [17], and phase-field method [9]. Only in the recent decade numerical schemes have been developed to describe fluid–structure interactions in level-set methods [12,22,16] and volume-of-fluid methods [28].

Phase-field models provide an alternative interface capturing approach, where an auxiliary field variable ϕ, the phase-field, is introduced and used to indicate the phases, e.g., $\phi = 1$ in the solid and $\phi = -1$ in the fluid. The phase-field function varies smoothly between these distinct values across the interface, resulting in a small but finite interface thickness. Depending on the application of interest, phase-field methods offer some distinct advantages over other interface capturing methods. For example, they can intrinsically include mass conservation and transport stabilization and allow for fully discrete energy stable schemes, see e.g. [5,14], for two-phase flows. Further these methods offer a simple mechanism to couple the multi-phase system to additional physical processes, for example on the interface or in the bulk phases, see for examples [24,8,15]. In case of a non-negligible surface energy, phase-field methods allow for a monolithic coupling of interface advection and flow equations, which can prevent time step restrictions due to stiff interfacial forces [4].

While phase-field methods are state-of-the-art for multi-phase flow problems, only one preliminary approach has been made to provide a phase-field model for FSI [29]. This might be due to the fact, that the interface in phase-field methods is diffuse with a finite thickness, making it harder to combine the solid and the fluid material in a consistent way. Here, we present an improved phase-field method for fluid–structure-interaction along with analytical and numerical validation. The resulting model shows some similarities with a previously introduced model for biofilms [30], which however was only designed for purely viscoelastic materials and cannot handle separated elastic and viscous phases as they occur in FSI problems.

We start by recapitulating the sharp interface equations for FSI in Sec. 2.1. The equations are extended to a phase-field formulation in Sec. 2.2. The model is based on a thermodynamically consistent derivation (Sec. 2.3). We provide a formal sharp interface limit showing convergence of the derived equations to traditional FSI formulations (Sec. 3). Numerical tests are presented in Sec. 4. Special focus is put on a comparison to the ALE reference solution of an elastic cell traversing a cylindrical channel. After this validation, we demonstrate the potential of the method in Sec. 5, by simulating

(i) a solid object moving through a fluidic channel without grid remeshing,
(ii) FSI with strong surface energy, i.e. surface tension forces,
(iii) contact dynamics of a bouncing ball, and
(iv) adhesion of an elastic object to a rigid wall.

The paper closes with conclusions on the applicability of the method in Sec. 6.

2. Phase-field model for FSI

2.1. Sharp interface model

Before deriving the phase-field model, let us begin by presenting the sharp interface equations for FSI. Let the computational domain $\Omega \subseteq \mathbb{R}^n$ be divided into a fluid domain and a solid domain. To be consistent with the later phase-field model, we call these domains Ω_{-1}(fluid) and Ω_1(solid). We introduce a common velocity field $\mathbf{v} : \Omega \to \mathbb{R}^n$ to indicate movements of the fluid and the solid material. Further, let us denote the material derivative by $\partial^\bullet = \partial_t + \mathbf{v} \cdot \nabla$. Throughout this work, we consider incompressible elastic materials, i.e. of $1/2$ Poisson ratio. The generalization to compressible solids should be possible by relaxing the incompressibility condition and including a bulk modulus, but is left for further studies. Balance laws for mass and momentum yield the evolution equations

$$\partial^\bullet(\rho_i \mathbf{v}) = \nabla \cdot \mathbb{S}_i - \nabla p \qquad \text{in } \Omega_i \tag{2.1}$$

$$\nabla \cdot \mathbf{v} = 0 \qquad \text{in } \Omega_i \tag{2.2}$$

for $i = -1, 1$, where $\mathbf{v}, p, \mathbb{S}_i$ denote the velocity, pressure and phase-dependent stress.

To describe the elastic stress in the Eulerian framework we introduce the left Cauchy–Green strain tensor σ. The strain tensor is typically calculated from the deformation gradient tensor $\mathbf{F}$, as $\sigma = \mathbf{F}\mathbf{F}^T$. In our phase-field approach we will have no access to the initial coordinates of a material point to calculate $\mathbf{F}$. Instead, we use the identity $\partial^\bullet \mathbf{F} = \nabla \mathbf{v}^T \mathbf{F}$ (see, e.g., [10]) from which one can easily compute the following evolution equation for σ,

$$\partial^\bullet \sigma - \nabla \mathbf{v}^T \cdot \sigma - \sigma \cdot \nabla \mathbf{v} = 0 \qquad \text{in } \Omega_1. \tag{2.3}$$

Note, that we use a row-wise nabla operator, i.e. $(\sigma \cdot \nabla \mathbf{v})_{ij} = \sigma_{ik} \partial_k \mathbf{v}_j$. The left-hand side of Eq. (2.3) is also known as the upper-convected Maxwell time derivative that rotates and stretches with the deformation. The initial condition for Eq. (2.3) is given by the strain in the undeformed configuration $\sigma = \mathbb{I}$, where $\mathbb{I}$ is the identity matrix. The corresponding elastic stress for a hyperelastic neo-Hookean material is given by $\mu_1(\sigma - \mathbb{I})$, where μ_1 is the shear modulus. In a fluid, the elastic stress vanishes since there is no strain, i.e.

$$\sigma = \mathbb{I} \qquad \text{in } \Omega_{-1} \tag{2.4}$$

for all times. The total phase-dependent stress is then given by the elastic stress plus a viscous part,

$$\mathbb{S}_i = \nu_i(\nabla \mathbf{v} + \nabla \mathbf{v}^T) + \mu_i(\sigma - \mathbb{I}) \tag{2.5}$$

where ν_i is the viscosity and μ_i is the shear modulus of the respective phase. In particular $\mu_{-1} = 0$ in a purely viscous fluid, and $\nu_1 = 0$ if the elastic solid has no additional viscosity.

Finally two jump conditions are specified at the fluid/solid interface,

$$[\mathbf{v}]_-^+ = 0, \qquad -[\mathbb{S}]_-^+ \cdot \mathbf{n} + [p]_-^+ \mathbf{n} = \gamma \kappa \mathbf{n}, \tag{2.6}$$

where $[f]_-^+ = f_{+1} - f_{-1}$ denotes the jump in f across the interface and $\mathbf{n}$ is the normal to Ω_1. The first condition is the continuity of the velocity. The second condition is the interfacial force balance including a possible surface tension force at the fluid/solid interface with surface tension γ and total curvature κ.

2.2. Phase-field modeling

Let ϕ denote a phase-field that distinguishes between the fluid domain ($\phi \approx -1$) and the solid domain ($\phi \approx 1$) within a computational domain Ω. Hence Ω_i is approximated by the domain where $\phi \approx i$. Since the phase-field approach allows mixing of the two domains to a certain degree, we define the velocity field now to be the volume-averaged velocity of this mixture, see [1] for details. The density is chosen as a linear combination of the densities in the two phases: $\rho(\phi) = \rho_1(1+\phi)/2 + \rho_{-1}(1-\phi)/2$. Balance laws for mass and momentum yield the evolution equations for phase-field and velocity:

$$\partial^\bullet \phi = -\nabla \cdot \mathbf{J} \qquad \text{in } \Omega \tag{2.7}$$

$$\partial^\bullet (\rho(\phi)\mathbf{v}) = \nabla \cdot \mathbb{S}(\phi) - \nabla p + \mathbf{F} \qquad \text{in } \Omega \tag{2.8}$$

$$\nabla \cdot \mathbf{v} = 0 \qquad \text{in } \Omega \tag{2.9}$$

where the stress depends now on the phase-field and the force $\mathbf{F}$ and flux $\mathbf{J}$ are specified later to meet the requirement of non-increasing energy.

To obtain an equation for the diffuse elastic strain tensor, we need to combine Eqs. (2.4) and (2.3). A typical approach in phase-field modeling is to multiply an equation with a characteristic function of its domain (here: Ω_{-1} or Ω_1) and to extend the domain then to the larger computational domain (here: Ω), see [23]. We follow a similar approach here and multiply Eq. (2.4) with a function $\alpha(\phi)$ and Eq. (2.3) with a function $\lambda(\phi)$. Adding up both results, we obtain the common equation for the diffuse elastic strain tensor as

$$\lambda(\phi)\left(\partial^\bullet \sigma - \nabla \mathbf{v}^T \cdot \sigma - \sigma \cdot \nabla \mathbf{v}\right) + \alpha(\phi)(\sigma - \mathbb{I}) = 0. \tag{2.10}$$

For $\alpha = 0$ the equation reduces to the strain evolution for an elastic solid (2.3), while for $\lambda = 0$ it reduces to the strain description of a fluid, i.e. Eq. (2.4). In case $\alpha = 1$, Eq. (2.10) is also known as Oldroyd-B equation. This equation is used to describe Maxwell-type visco-elasticity with λ being the relaxation time controlling the dissipation of elastic stress. The above generalization of the Oldroyd-B equation to arbitrary α, leads to the relaxation time λ/α. Note, that this ratio is the only free (spatially varying) parameter of Eq. (2.10), but the introduction of α effectively allows to choose this ratio equal to infinity in some region of the computational domain by setting $\alpha = 0$ there.

The total phase-dependent stress is then given by the elastic stress plus a viscous part,

$$\mathbb{S}(\phi) = \nu(\phi)(\nabla \mathbf{v} + \nabla \mathbf{v}^T) + \mu(\phi)(\sigma - \mathbb{I}) \tag{2.11}$$

where $\nu(\phi)$ is the viscosity and $\mu(\phi)$ is the shear modulus of the respective phase. We use linear interpolations for all phase-dependent quantities,

Table 1
Different material laws can be obtained by different choice of parameters. The star symbol '$*$' marks parameters that are given by the physical problem itself, T indicates the characteristic time scale of the given problem.

Viscosity $\nu(\phi)$	Shear modulus $\mu(\phi)$	Relax. time		Corresponding material
		$\lambda(\phi)$	$\alpha(\phi)$	
$*$	0	0	1	Viscous fluid
0	$*$	T	0	Elastic solid
$*$	$*$	T	0	Visco-elastic Kelvin–Voigt
0	$*$	$*$	1	Visco-elastic Maxwell

$$\mu(\phi) = \mu_1(1+\phi)/2 + \mu_{-1}(1-\phi)/2$$
$$\nu(\phi) = \nu_1(1+\phi)/2 + \nu_{-1}(1-\phi)/2$$
$$\lambda(\phi) = \lambda_1(1+\phi)/2 + \lambda_{-1}(1-\phi)/2$$
$$\alpha(\phi) = \alpha_1(1+\phi)/2 + \alpha_{-1}(1-\phi)/2$$

Hence to model interaction of a solid ($\phi = 1$) with a fluid ($\phi = -1$), we insert the given physical parameters for elastic shear modulus μ_1, the fluid viscosity ν_{-1} and set $\mu_{-1} = \nu_1 = \alpha_1 = \lambda_{-1} = 0$. It remains to specify α_{-1} and λ_1 which can be interpreted to control the relaxation time in the diffuse interface region where a mixture of fluid and elastic phase is present. Note, that due to the structure of Eq. (2.10) the only free parameter here is the ratio λ_1/α_{-1}, which we can also think of an interface relaxation time. Obviously, this time has to be scaled somehow with the characteristic time scale T of the considered problem, which suggests to simply use $\lambda_1/\alpha_{-1} = T$, for example by setting $\alpha = 1, \lambda = T$. This parameter choice will also be numerically tested in Sec. 4.3.

An overview of the parameters can be found in Table 1. Note, that also visco-elastic material phases can be modeled. For Kelvin–Voigt visco-elasticity it suffices to add a viscosity inside of the elastic material. For Maxwell visco-elasticity one can just prescribe the Maxwell relaxation time for λ. Hence, any combination of two phases, be it viscous, visco-elastic or solid, can be modeled by choosing the parameters as given in Table 1.

2.3. Energy dissipation

To close the system of equations, it remains to specify the flux $\mathbf{J}$ and force $\mathbf{F}$ to obtain a thermodynamically consistent evolution. We define the total energy E of the system as sum of kinetic, elastic [11] and diffuse surface energy [2] as follows,

$$E = \int_\Omega \frac{\rho(\phi)}{2}|\mathbf{v}|^2 + \frac{\mu(\phi)}{2}\mathrm{tr}\,(\sigma - \ln\sigma - \mathbb{I}) + \tilde{\gamma}\left(\frac{\epsilon}{2}|\nabla\phi|^2 + \frac{1}{\epsilon}W(\phi)\right)\mathrm{d}x. \tag{2.12}$$

Here, '$\mathrm{tr}(A)$' is the trace of a matrix A, ϵ the interface thickness, W a double-well potential and $\tilde{\gamma}$ a (scaled) surface tension, whose scaling depends on the choice of W. Here, we choose $W(\phi) = \frac{1}{4}(1-\phi^2)^2$ which leads to $\tilde{\gamma} = \frac{3}{2\sqrt{2}}\cdot\gamma$, see e.g. [3, Sec. 2.2]. Inserting (2.8)–(2.11) into Eq. (2.12) we can compute the time evolution of the energy. The complete computation is carried out in the appendix. We obtain

$$\begin{aligned}\frac{d}{dt}E = \int_\Omega &-\frac{\nu(\phi)}{2}\left|\nabla\mathbf{v} + \nabla\mathbf{v}^T\right|^2 + \mathbf{J}\cdot\nabla\left[\frac{\mu'(\phi)}{2}\mathrm{tr}(\sigma - \ln\sigma - \mathbb{I}) + \tilde{\gamma}\left(\frac{1}{\epsilon}W'(\phi) - \epsilon\Delta\phi\right)\right]\\ &+ \mathbf{v}\cdot\left[\mathbf{F} + \nabla\cdot(\rho'(\phi)\mathbf{v}\otimes\mathbf{J}) + \epsilon\tilde{\gamma}\nabla\cdot(\nabla\phi\otimes\nabla\phi)\right]\mathrm{d}x - \int_{\Omega\setminus\{\lambda=0\}}\frac{\mu(\phi)\alpha(\phi)}{2\lambda(\phi)}\mathrm{tr}(\sigma + \sigma^{-1} - 2\mathbb{I})\,\mathrm{d}x\end{aligned} \tag{2.13}$$

under appropriate boundary conditions. Note, that the last term is non-negative for any given tensor σ and bounded as explained in Sec. A.1. Hence, with the choice

$$\mathbf{F} = -\nabla\cdot(\rho'(\phi)\mathbf{v}\otimes\mathbf{J}) - \epsilon\tilde{\gamma}\nabla\cdot(\nabla\phi\otimes\nabla\phi), \tag{2.14}$$
$$\mathbf{J} = -m(\phi)\nabla\left[\frac{\mu'(\phi)}{2}\mathrm{tr}(\sigma - \ln\sigma - \mathbb{I}) + \tilde{\gamma}\left(\frac{1}{\epsilon}W'(\phi) - \epsilon\Delta\phi\right)\right] \tag{2.15}$$

for some mobility function $m(\phi) > 0$, we obtain non-increasing energy,

$$\frac{d}{dt}E = -\int_\Omega \frac{\nu(\phi)}{2}\left|\nabla\mathbf{v} + \nabla\mathbf{v}^T\right|^2 + \frac{1}{m(\phi)}|\mathbf{J}|^2\,\mathrm{d}x - \int_{\Omega\setminus\{\lambda=0\}}\frac{\mu(\phi)\alpha(\phi)}{2\lambda(\phi)}\mathrm{tr}(\sigma + \sigma^{-1} - 2\mathbb{I})\,\mathrm{d}x \le 0.$$

2.4. Governing equations

In the following we summarize the governing equations for the thermodynamically consistent visco-elastic phase-field model. As noted earlier, the model can be used to describe any combination of viscous, visco-elastic and elastic materials, by choosing the parameters accordingly, see Table 1.

$$\partial^\bullet(\rho(\phi)\mathbf{v}) + \frac{\rho_{-1}-\rho_1}{2}\nabla\cdot(\mathbf{v}\otimes m(\phi)\nabla q) \tag{2.16}$$
$$-\nabla\cdot\left(\nu(\phi)\left(\nabla\mathbf{v}+\nabla\mathbf{v}^T\right)+\mu(\phi)\,(\sigma-\mathbb{I})\right)+\nabla p = -\tilde{\gamma}\epsilon\nabla\cdot(\nabla\phi\otimes\nabla\phi)\,,$$
$$\nabla\cdot\mathbf{v}=0, \tag{2.17}$$
$$\partial^\bullet\phi = \nabla\cdot(m(\phi)\nabla q)\,, \tag{2.18}$$
$$\frac{\mu'(\phi)}{2}\mathrm{tr}(\sigma-\ln\sigma-\mathbb{I})+\tilde{\gamma}\left(\frac{1}{\epsilon}W'(\phi)-\epsilon\Delta\phi\right)=q, \tag{2.19}$$
$$\lambda(\phi)\left(\partial^\bullet\sigma-\nabla\mathbf{v}^T\cdot\sigma-\sigma\cdot\nabla\mathbf{v}\right)+\alpha(\phi)(\sigma-\mathbb{I})=0. \tag{2.20}$$

In numerical tests we find, that if the chemical potential q as defined in Eq. (2.19) is used in the evolution equation of the phase-field, the resulting ϕ does not provide a good description of the interface layer because of the contributions of the elastic strain. Since the primary purpose of ϕ is to track the two-phase interface, we use a simplified version of the q in the numerical simulations, which omits the strain-dependent terms,

$$q=\frac{1}{\epsilon}W'(\phi)-\epsilon\Delta\phi \tag{2.21}$$

replacing Eq. (2.19). This amounts into a classical advected Cahn–Hilliard equation for ϕ, which is now also independent of the surface tension. Note that the resulting system is no longer variational and does not necessarily decrease the energy. However, this effect tends to be higher order since, if Eq. (2.21) is used, away from the interface $W'(\phi)=\Delta\phi=0$ and near the interface ϕ locally equilibrates yielding $W'(\phi)\approx\epsilon^2\Delta\phi$ and thus $q\approx 0$. Note that if $q=0$, then the energy is non-increasing, $\frac{d}{dt}E\le 0$ which follows from Eq. (2.13).

In the following section we derive relations of our phase-field model in the sharp interface limit (i.e. $\epsilon\to 0$) with the aid of formal asymptotic expansions. We perform the analysis for the full model containing the strain dependent terms in q, but we will see that the asymptotic analysis holds equally for the simplified model involving Eq. (2.21).

3. Sharp interface asymptotics

In the following we only consider the case $\lambda(-1)=0,\alpha(-1)=0,\lambda(1)=T>0,\alpha(1)=0$, which corresponds to the coupling of a viscous fluid and an elastic solid. Following [1], we perform formally matched asymptotic expansions. Therefore we consider a solution $(\mathbf{v},p,\phi,q,\sigma)$ of the system given by Eqs. (2.16)–(2.20). For the mobility m we distinguish two cases in the following:

$$m(\phi)=\begin{cases}\epsilon m_0 & \text{case I}\,,\\ m_1(1-\phi^2)_+ & \text{case II}\end{cases}$$

where $m_0,m_1>0$ are constants and $(.)_+$ is the positive part of the quantity in the brackets. A lot of calculations and arguments follow closely [1] with suitable modifications. For the convenience of the reader we include them in detail although some are the same as in [1].

3.1. Outer expansions

The first step is to expand the solution in regions away from the interface. Therefore we assume an expansion of the form

$$\mathbf{v}^\epsilon=\sum_{k=0}^{\infty}\epsilon^k\mathbf{v}_k,\ \phi^\epsilon=\sum_{k=0}^{\infty}\epsilon^k\phi_k,\ \ldots. \tag{3.1}$$

An expansion of Eq. (2.21) at order $\frac{1}{\epsilon}$ leads to $W'(\phi_0)=0$, which yields the stable solutions $\phi_0=\pm 1$. Expanding the Eq. (2.16) we obtain

$$\partial^\bullet(\rho_i \mathbf{v}_0) - \nabla\cdot\left(\nu_i\left(\nabla\mathbf{v}_0 + \nabla\mathbf{v}_0^T\right) + \mu_i\sigma_0\right) + \nabla p_0 = 0 \quad \text{in } \Omega_i, \tag{3.2}$$

$$\nabla\cdot\mathbf{v}_0 = 0 \quad \text{in } \Omega_i, \tag{3.3}$$

$$\sigma_0 = \mathbb{I} \quad \text{in } \Omega_{-1}, \tag{3.4}$$

$$\partial^\bullet\sigma_0 - \nabla\mathbf{v}_0^T\cdot\sigma_0 - \sigma_0\cdot\nabla\mathbf{v}_0 = 0 \quad \text{in } \Omega_1, \tag{3.5}$$

where $i = -1, 1$ and Ω_i the domain where $\phi_0 = i$. Furthermore we denoted by $\rho_{\pm1} = \rho(\pm1)$, $\nu_{\pm1} = \nu(\pm1)$ and $\mu_{\pm1} = \mu(\pm1)$. Note that we recover the sharp interface equations given in Sec. 2.1.

3.2. Inner expansions

As a second step we prepare the expansion in the interface region and therefore introduce new coordinates in a neighborhood of the smoothly evolving interface $\Gamma = \Gamma(t)$, $t \geq 0$. We define a local parameterization of Γ by

$$\boldsymbol{\zeta} : I \times U \to \mathbb{R}^n \tag{3.6}$$

with a time interval $I \subset \mathbb{R}$ and a spatial parameter domain $U \subset \mathbb{R}^{n-1}$. The unit normal to $\Gamma(t)$ will be denoted by $\mathbf{n}$ and points into Ω_1. In the following we adopt the notation from [1]. We consider the signed distance function $d(t,x)$ of a point x to the sharp interface $\Gamma^0(t)$ with $d(t,x) > 0$ if $x \in \Omega_1(t)$. In addition, we denote by $z = \frac{d}{\epsilon}$ a rescaled distance. We now introduce the new coordinates by defining a local parameterization of $I \times \mathbb{R}^n$ close to $\boldsymbol{\zeta}(I \times U)$ as follows:

$$G^\epsilon(t,s,z) = (t, \boldsymbol{\zeta}(t,s) + \epsilon z\mathbf{n}(t,s)) \tag{3.7}$$

with $s \in U$. It will turn out that we need the following identities, containing a scalar function $b(t,x)$ and a vector field $\mathbf{j}(t,x)$:

$$\frac{d}{dt}b(t,x) = -\frac{1}{\epsilon}\mathcal{V}\partial_z\hat{b} + \text{ h.o.t.}, \tag{3.8}$$

$$\nabla_x b = \nabla_{\Gamma_{\epsilon z}}\hat{b} + \frac{1}{\epsilon}\partial_z\hat{b}\,\mathbf{n}, \tag{3.9}$$

$$\nabla_x\cdot\mathbf{j} = \mathrm{div}_{\Gamma_{\epsilon z}}\hat{\mathbf{j}} + \frac{1}{\epsilon}\partial_z\hat{\mathbf{j}}\cdot\mathbf{n}, \tag{3.10}$$

with the correspondences

- $\hat{b}$ is the denotation of b in the new coordinates with $\hat{b}(t, s(t,x), z(t,x)) = b(t,x)$.
- $\mathcal{V} = \partial_t\boldsymbol{\zeta}\cdot\mathbf{n}$ is the scalar normal velocity.
- h.o.t. stands for higher order terms as $\varepsilon \to 0$.
- ∇_x is the gradient with respect to the spatial variables.
- $\nabla_{\Gamma_{\epsilon z}}$ is the surface gradient on $\Gamma_{\epsilon z} := \{\boldsymbol{\zeta}(s) + \epsilon z\mathbf{n}(s) \mid s \in U\}$.
- $\mathrm{div}_{\Gamma_{\epsilon z}}\hat{\mathbf{j}}$ is the divergence of $\hat{\mathbf{j}}$ on $\Gamma_{\epsilon z}$.
- κ is the total curvature of $\Gamma(t)$.
- $|\mathcal{S}|$ is the spectral norm of the Weingarten map $\mathcal{S}$ of $\Gamma(t)$,

cf. [1]. Note, that we omit the time dependence in the following argumentations, as done for $\Gamma_{\epsilon z}$ above. Moreover, we will make use of the relations (see Appendix of [1])

$$\nabla_{\Gamma_{\epsilon z}}\hat{b}(s,z) = \nabla_\Gamma\hat{b}(s,z) + \text{ h.o.t.},$$
$$\mathrm{div}_{\Gamma_{\epsilon z}}\hat{\mathbf{j}}(s,z) = \mathrm{div}_\Gamma\hat{\mathbf{j}}(s,z) + \text{ h.o.t.},$$
$$\Delta_{\Gamma_{\epsilon z}}\hat{b}(s,z) = \Delta_\Gamma\hat{b}(s,z) + \text{ h.o.t.},$$

where $\nabla_\Gamma, \mathrm{div}_\Gamma, \Delta_\Gamma$ are the respective surface operators on Γ.

3.3. Matching conditions

As for the outer variables, we now assume an ϵ-series approximation for the unknown functions $(\mathbf{V}, P, \Phi, Q, \Sigma)$ in the inner variables:

$$\mathbf{V}^\epsilon = \sum_{k=0}^{\infty}\epsilon^k\mathbf{V}_k, \quad \Phi^\epsilon = \sum_{k=0}^{\infty}\epsilon^k\Phi_k, \quad \dots .$$

Representatively, we obtain the following matching conditions for the phase field function at $x = \boldsymbol{\zeta}(s)$:

$$\lim_{z\to\pm\infty}\Phi_0(z,s)=\phi_0(x\pm)\,,\qquad \lim_{z\to\pm\infty}\partial_z\Phi_0(z,s)=0 \tag{3.11}$$

$$\lim_{z\to\pm\infty}\partial_z\Phi_1(z,s)=\nabla\phi_0(x\pm)\cdot\mathbf{n}\,, \tag{3.12}$$

where $\phi_0(x\pm)$ denotes the limit $\lim_{\delta\searrow 0}\phi_0(x\pm\delta\mathbf{n})$.

3.4. The equations to leading order

We insert the asymptotic expansions into Eqs. (2.16)–(2.20) and ask that each individual coefficient of a power in ϵ vanishes. The leading order of equation (2.19) is $\frac{1}{\epsilon}$, which gives

$$0=\partial_{zz}\Phi_0-W'(\Phi_0). \tag{3.13}$$

Using (3.11) we obtain

$$\Phi_0(z)\to\pm 1\quad\text{for}\quad z\to\pm\infty\,. \tag{3.14}$$

We now assume additionally that

$$\Phi_0(0)=0\,.$$

Together with this condition (3.13), (3.14) has a unique solution. Hence Φ_0 does not depend on t and s. The leading order of Equation (2.17) yields

$$\partial_z\mathbf{V}_0\cdot\mathbf{n}=\partial_z(\mathbf{V}_0\cdot\mathbf{n})=0\,. \tag{3.15}$$

The matching condition implies that $(\mathbf{V}_0\cdot\mathbf{n})(z)$ is bounded. Hence

$$(\mathbf{v}_0\cdot\mathbf{n})(x+)=\lim_{z\to\infty}(\mathbf{V}_0\cdot\mathbf{n})(z)=\lim_{z\to-\infty}(\mathbf{V}_0\cdot\mathbf{n})(z)=(\mathbf{v}_0\cdot\mathbf{n})(x-)\,.$$

Thus

$$[\mathbf{v}_0\cdot\mathbf{n}]_-^+=0\,,$$

where $[u]_-^+(x)=u(x+)-u(x-)$ denotes the jump of a quantity at the interface.

For the analysis of Eq. (2.18) we have to distinguish the different case for the mobility.

Case I: $m(\phi)=\epsilon m_0$.

Equating the order $\frac{1}{\epsilon}$ term we obtain from Eq. (2.18)

$$-\mathcal{V}\partial_z\Phi_0+(\mathbf{V}_0\cdot\mathbf{n})\partial_z\Phi_0=\partial_z(m_0\partial_z Q_0\mathbf{n})\cdot\mathbf{n}=m_0\partial_{zz}Q_0\,. \tag{3.16}$$

Moreover, matching yields

$$\partial_z Q_0\to 0\quad\text{for}\quad z\to\pm\infty\,,$$

cf. (3.11). If we integrate (3.16) with respect to z, we obtain

$$\mathcal{V}=\mathbf{v}_0\cdot\mathbf{n}\,.$$

Since $\partial_{zz}Q_0=0$, we conclude that Q_0 is independent of z.

Case II: $m(\phi)=m_1(1-\phi^2)_+$.

Equating the order $\frac{1}{\epsilon^2}$ terms, we obtain

$$0=\partial_z(m_1(1-\Phi_0^2)\partial_z Q_0\mathbf{n})\cdot\mathbf{n}=\partial_z(m_1(1-\Phi_0^2)\partial_z Q_0)\,.$$

Moreover, matching yields

$$m_1(1-\Phi_0^2)\partial_z Q_0\to 0\quad\text{for}\quad z\to\pm\infty$$

and therefore

$$m_1(1-\Phi_0^2)\partial_z Q_0\equiv 0,$$

which implies

$$Q_0 = Q_0(s,t)\,.$$

At order $\frac{1}{\epsilon}$ we obtain

$$-\mathcal{V}\partial_z\Phi_0 + (\mathbf{V}_0)\cdot\mathbf{n}\partial_z\Phi_0 = 0.$$

As before integration yields $\mathcal{V} = \mathbf{v}_0\cdot\mathbf{n}$.

Next we discuss the equation for the conservation of linear momentum. Application of Eq. (3.9) for each component yields

$$\begin{aligned}\nabla_x\mathbf{v} &= \tfrac{1}{\epsilon}\partial_z\mathbf{V}\otimes\mathbf{n} + \nabla_{\Gamma_{\epsilon z}}\mathbf{V}\,,\\ \nabla_x\mathbf{v} + \nabla_x\mathbf{v}^T &= \tfrac{1}{\epsilon}(\partial_z\mathbf{V}\otimes\mathbf{n} + \mathbf{n}\otimes\partial_z\mathbf{V}) + (\nabla_{\Gamma_{\epsilon z}}\mathbf{V} + (\nabla_{\Gamma_{\epsilon z}}\mathbf{V})^\top)\,.\end{aligned}$$

For the following we define $\mathcal{E}(\mathbf{A}) = \frac{1}{2}(\mathbf{A}+\mathbf{A}^\top)$ for a quadratic matrix $\mathbf{A}$. Hence

$$\begin{aligned}\nabla_x\cdot(\nu(\phi)(\nabla_x\mathbf{v}+\nabla_x\mathbf{v}^T)) &= \tfrac{1}{\epsilon^2}\partial_z(2\nu(\Phi)\mathcal{E}(\partial_z\mathbf{V}\otimes\mathbf{n}))\mathbf{n} + \tfrac{1}{\epsilon}\partial_z(2\nu(\Phi)\mathcal{E}(\nabla_{\Gamma_{\epsilon z}}\mathbf{V}))\mathbf{n}\\ &\quad + \tfrac{1}{\epsilon}\nabla_{\Gamma_{\epsilon z}}\cdot(2\nu(\Phi)\mathcal{E}(\partial_z\mathbf{V}\otimes\mathbf{n})) + \nabla_{\Gamma_{\epsilon z}}\cdot(2\nu(\Phi)\mathcal{E}(\nabla_{\Gamma_{\epsilon z}}\mathbf{V}))\\ &= \tfrac{1}{\epsilon^2}\partial_z(2\nu(\Phi)\mathcal{E}(\partial_z\mathbf{V}\otimes\mathbf{n})\mathbf{n}) + \tfrac{1}{\epsilon}\partial_z(2\nu(\Phi)\mathcal{E}(\nabla_{\Gamma_{\epsilon z}}\mathbf{V})\mathbf{n})\\ &\quad + \tfrac{1}{\epsilon}\nabla_{\Gamma_{\epsilon z}}\cdot(2\nu(\Phi)\mathcal{E}(\partial_z\mathbf{V}\otimes\mathbf{n})) + \nabla_{\Gamma_{\epsilon z}}\cdot(2\nu(\Phi)\mathcal{E}(\nabla_{\Gamma_{\epsilon z}}\mathbf{V}))\,,\end{aligned}$$

where we used $\partial_z\mathbf{n} = 0$ as in [1]. We conclude from Eq. (3.15)

$$(\mathbf{n}\otimes\partial_z\mathbf{V}_0)\mathbf{n} = (\partial_z\mathbf{V}_0\cdot\mathbf{n})\mathbf{n} = 0\,.$$

Since Φ_0 is independent of t and s, Eq. (3.9) implies

$$\nabla\phi\otimes\nabla\phi = \tfrac{1}{\epsilon^2}(\partial_z\Phi_0)^2(\mathbf{n}\otimes\mathbf{n}) + \tfrac{2}{\epsilon}\partial_z\Phi_1\partial_z\Phi_0(\mathbf{n}\otimes\mathbf{n}) + \text{ h.o.t.}$$

Because of $(\nabla_\Gamma\mathbf{n})\mathbf{n} = 0$, we conclude

$$\epsilon\nabla\cdot(\nabla\phi\otimes\nabla\phi) = \tfrac{1}{\epsilon^2}\partial_z(\partial_z\Phi_0)^2\mathbf{n} + \tfrac{1}{\epsilon}(\partial_z\Phi_0)^2(\nabla_\Gamma\cdot\mathbf{n})\mathbf{n} + \tfrac{2}{\epsilon}\partial_z(\partial_z\Phi_1\partial_z\Phi_0)\mathbf{n} + \text{ h.o.t..}$$

Since the leading order of the chemical potential does not depend on z, the term $\operatorname{div}(\mathbf{v}\otimes m(\phi)\nabla q)$ gives no contribution to the order $\frac{1}{\epsilon^2}$. Therefore the order $\frac{1}{\epsilon^2}$ terms from the momentum equation yield

$$\tilde{\gamma}\,\partial_z(\partial_z\Phi_0)^2\mathbf{n} = \partial_z(\nu(\Phi_0)\partial_z\mathbf{V}_0)\,. \tag{3.17}$$

Taking the inner product of Eq. (3.17) with $\mathbf{n}$, using $\partial_z\mathbf{n} = 0$ and $\partial_z\mathbf{V}_0\cdot\mathbf{n} = 0$ yields

$$\tilde{\gamma}\,\partial_z((\partial_z\Phi_0)^2) = 0\,.$$

Therefore (3.17) implies

$$\partial_z(\nu(\Phi_0)\partial_z\mathbf{V}_0) = 0\,. \tag{3.18}$$

The matching conditions yield that $\mathbf{V}_0(z)$ is bounded. Thus Eq. (3.18) interpreted as an ODE in z has only solutions $\mathbf{V}_0$ which are constant in z. Again matching yields

$$[\mathbf{v}_0]_-^+ = 0\,. \tag{3.19}$$

Thus we recover the first part of the sharp interface jump condition in Eq. (2.6).

3.5. The momentum balance in the sharp interface limit

Now we analyze the momentum equation to the next order. The term $\nabla\cdot(\nu(\phi)D\mathbf{v})$ gives to the order $\frac{1}{\epsilon}$,

$$\partial_z(\nu(\Phi_0)\mathcal{E}(\partial_z\mathbf{V}_1\otimes\mathbf{n})\mathbf{n}) + \partial_z(\nu(\Phi_0)\mathcal{E}(\nabla_\Gamma\mathbf{V}_0)\mathbf{n})\,.$$

Because of the matching conditions, we require $\lim_{z\to\pm\infty}\partial_z\mathbf{V}_1(z) = \nabla\mathbf{v}_0(x\pm)\mathbf{n}$. Hence

$$\partial_z\mathbf{V}_1\otimes\mathbf{n} + \nabla_\Gamma\mathbf{V}_0 \to \nabla_x\mathbf{v} \quad \text{for} \quad z\to\pm\infty\,. \tag{3.20}$$

Moreover, the term $\operatorname{div}(\mathbf{v}\otimes m(\phi)\nabla q)$ gives no contribution to order $\frac{1}{\epsilon}$. Thus we obtain from the momentum equation at order $\frac{1}{\epsilon}$:

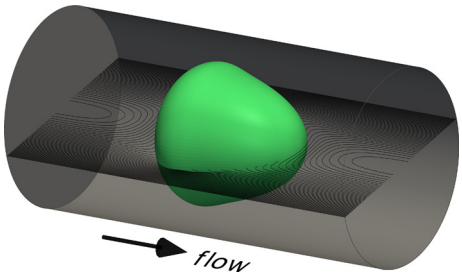

Fig. 1. Illustration of the simulated scenario. An initially spherical elastic cell (green) is deformed by pressure and shear forces as it flows through a fluid-filled cylindrical channel. Streamlines (black) visualize fluid movement relative to cell velocity. (For interpretation of the colors in the figure(s), the reader is referred to the web version of this article.)

$$
\begin{aligned}
&-\partial_z(\rho(\Phi_0)\mathbf{V}_0)\mathcal{V} + \partial_z(\rho(\Phi_0)(\mathbf{V}_0 \otimes \mathbf{V}_0))\mathbf{n} \\
&-2\partial_z(\nu(\Phi_0)\mathcal{E}(\partial_z\mathbf{V}_1 \otimes \mathbf{n})\mathbf{n}) - 2\partial_z(\nu(\Phi_0)\mathcal{E}(\nabla_\Gamma \mathbf{V}_0)\mathbf{n}) \\
&-\tilde{\gamma}(\partial_z\Phi_0)^2\kappa\mathbf{n} + \tilde{\gamma}\,\partial_z(2\partial_z\Phi_1\partial_z\Phi_0)\mathbf{n} + \partial_z(\mu(\Phi_0)\Sigma_0\mathbf{n}) + \partial_z P_0\mathbf{n} = 0
\end{aligned}
$$

because of $\kappa = -\operatorname{div}\mathbf{n}$. Integration with respect to z yields after matching and the use of Eq. (3.20)

$$
\begin{aligned}
&-[\rho_0\mathbf{v}_0]^+_-\mathcal{V} + [\rho_0\mathbf{v}_0]^+_-\mathbf{v}_0\cdot\mathbf{n} - 2[\nu\mathcal{E}(\nabla_x\mathbf{v}_0)]^+_-\mathbf{n} \\
&-\tilde{\gamma}\left(\int_{-\infty}^{\infty}(\partial_z\Phi_0)^2 dz\right)\kappa\mathbf{n} - [\mu(\phi_0)\sigma_0]^+_-\mathbf{n} + [p_0]^+_-\mathbf{n} = 0\,,
\end{aligned}
$$

where $k_\gamma := \int_{-\infty}^{\infty}(\partial_z\Phi_0)^2\,dz = \frac{4\sqrt{2}}{3}$ for our choice of W, see e.g. [3, Sec. 2.2]. Since $\mathbf{v}_0\cdot\mathbf{n} = \mathcal{V}$, we conclude

$$
-2[\nu D\mathbf{v}_0]^+_-\mathbf{n} + [p_0]^+_-\mathbf{n} - [\mu(\phi_0)\sigma_0]^+_-\mathbf{n} = \gamma\kappa\mathbf{n}\,, \tag{3.21}
$$

since $\gamma = k_\gamma\tilde{\gamma}$. Therefore we recover the second part of the sharp interface jump condition in Eq. (2.6).

4. Numerical tests

Numerical tests are indispensable to validate numerical models and to assess their accuracy. Nowadays, the standard benchmark for fluid–structure-interaction is the FeatFlow benchmark [31] where a channel flow induces oscillations of a thin elastic bar attached to a rigid object. Obviously, the phase-field model is not well suited to represent such a thin structure, since the corresponding interface thickness would be required to be much thinner than the structure itself, resulting in an extremely fine grid and very high computational costs. Consequently, we choose a different benchmark system serving the current purpose of testing the phase-field model in a practically relevant situation.

We consider the flow of a deforming solid ball through a fluid-filled channel. Firstly, this highlights the ability of interface capturing methods to account for movements of the solid and fluid domains with respect to each other. Secondly, the test scenario is based on a physically relevant simulation of biological cells traversing a flow channel. Cells are approximated as homogeneous incompressible elastic solids surrounded by a cortex with an active surface tension. While we neglect this active tension in the benchmark stage, we will add it to the model later to illustrate the opportunity of phase field models to stabilize the stiffness arising between interface advection and surface forces [4].

Note, that many typical modeling approaches consider cells as fluid-filled elastic membranes, see for example [6] for phase field methods, or [21] for a Lattice Boltzmann method. While the approximation as a membrane is a valid choice for red blood cells whose bulk is relatively soft, our focus here is on most other animal cell types whose mechanical response is dominated by the elasticity of the cell bulk. Such cells are also often immersed in a liquid environment in biological processes as well as in biotechnical applications, for example for ultra-fast identification of cell mechanical properties [25], which serves as a reference for this benchmark.

4.1. Test setup

We simulate the flow of an initially spherical solid object, also called *cell*, through a fluid-filled channel. To be consistent with the reference simulations [25], we consider the solid object and the channel to be axisymmetric. Axisymmetry effectively reduces the problem to a two-dimensional flow with axisymmetric operators. Hence, we consider a two-dimensional rectangular domain Ω whose lower boundary represents the symmetry axis, see Fig. 8 for an illustration. Here, $\Omega = [0, 40]\ \mu\text{m} \times [0, 10]\ \mu\text{m}$ which corresponds to a cylindrical channel of radius 10 µm, see Fig. 1 for an illustration.

Periodic boundary conditions are used at channel inlet and outlet for all fields but the pressure, which effectively leads to a channel of infinite length. A pressure difference between the channel inlet and outlet is imposed to drive the flow. The

Fig. 2. Cell shape at different times for $E = 6$ kPa, $r = 6$ μm, which corresponds to the parameter set discussed in Fig. 3. Remarkable changes of the shape occur within the first 100 μs. The last image compares the stationary shape of the phase-field method with the ALE reference shape (black crosses).

initial pressure difference is 2500 Pa. This pressure difference is adapted during the simulation such that a constant flow rate of 4e−11 m^3/s appears, see [25] for details on the adaption algorithm. At the channel wall, we impose no slip ($\mathbf{v} = 0$) for the velocity and no flux for the Cahn–Hilliard system.

Surface tension forces are neglected at first, since we aim to benchmark the fluid–structure part of the method. Moreover, we choose the following physical parameters for our simulations: $\nu_1 = \nu_{-1} = 10$ Pa·s, $\rho_1 = \rho_{-1} = 1000 \frac{\text{kg}}{\text{m}^3}$, $\mu_{-1} = 0$. The shear modulus of the cell, μ_1 is related to its Young's modulus E by $E = 3\mu_1$. Different values of E are used in the tests. The radius of the initially spherical cell is set to $r = 6$ μm.

Unless otherwise stated, the standard model parameters are $\epsilon = 0.0125$ μm and constant mobility $m = 10^{-8}$ m^3 s/kg. The characteristic time scale of the considered problem is approximately $T = 1$ ms, we choose the parameters for the Oldroyd-B equation accordingly $\alpha_1 = 0$, $\alpha_{-1} = 1$, $\lambda_1 = 1$ ms, $\lambda_{-1} = 0$, as suggested in Table 1. Note, that the only free parameter here is λ_1, we will later assess the influence of variations in λ_1 in our numerical tests.

The problem is discretized in the finite element toolbox AMDiS [32,33]. We chose an adaptive mesh refinement strategy. Coarsening and refinement of the mesh are controlled by the phase-field function such that the region $\phi \in [-0.9, 0.9]$ is resolved by at least five degrees of freedom across the interface. Away from the interface the fixed grid size $h = 0.625$ μm is chosen.

P1 finite elements are used for the pressure and P2 elements for the other variables. The time discretization is based on an implicit Euler method. Thereby, the Navier–Stokes and Cahn–Hilliard system are monolithically coupled while the Oldroyd-B equation (2.10) is solved separately in each time step. For details on the axisymmetric equations and the time discretization we refer to the Appendix A.2.

4.2. Benchmark quantity

After being deformed by pressure and shear forces, the solid will assume a stationary shape whereupon its flow becomes purely translational. We aim in particular to reproduce this state of stationary deformation. Note that this is a highly challenging problem for a phase-field method, since the structure needs to resist any movement, while the fluid keeps flowing around it and continuous movement takes place, even in the diffuse interface.

We introduce the deformation as a measure of the deviation of the cell shape from a circle,

$$d = 1 - \text{circularity} = 1 - \frac{2\sqrt{A\pi}}{P},$$

where A and P denote the area and the perimeter of the 2D view of the deformed object, measured by a piecewise linear approximation of the zero-level of ϕ. It has been shown in [25] that d is a delicate measure of the cell shape that can be uniquely related to the exact elastic modulus of the cell. We hence use this quantity as a main indicator for comparison of the phase-field model with the ALE reference solution.

Reference values for the stationary cell shapes are given in [25] for various cell sizes, flow rates and elastic moduli. There, an ALE method was employed using a co-moving grid to keep the cell in the center of the computational domain throughout the simulation. The data in [25] has been shown to be extremely accurate in terms of spatial and temporal discretization errors and has been widely used for comparisons to corresponding experiments. The experimental technique, called Real-Time-Deformability Cytometry (RT-DC), can be used to probe mechanical properties of biological cells in flow [26]. A validation study with purely elastic spherical particles showed very good agreement between ALE simulations and experiments.

4.3. Simulation results

In this section we compare the phase-field method presented in this paper with the ALE reference data and perform a parameter study to justify our choice of λ_1, ϵ and m, respectively.

Fig. 1 provides an idea of the actually simulated 3D scenario. It illustrates a stationary state shape in the cylinder, together with the streamlines of the flow. Fig. 2 shows the cell shape for different times. The initially spherical cell deforms due to fluid pressure and shear forces until it assumes a quasi-stationary state. A comparison with the ALE reference shape shows excellent agreement (Fig. 2, right).

Fig. 3 shows the corresponding evolution of the cell deformation. In 3(a) we investigate the dependence of the deformation evolution on the interface width ϵ. The deformation decreases for decreasing ϵ, for the smallest values of ϵ we

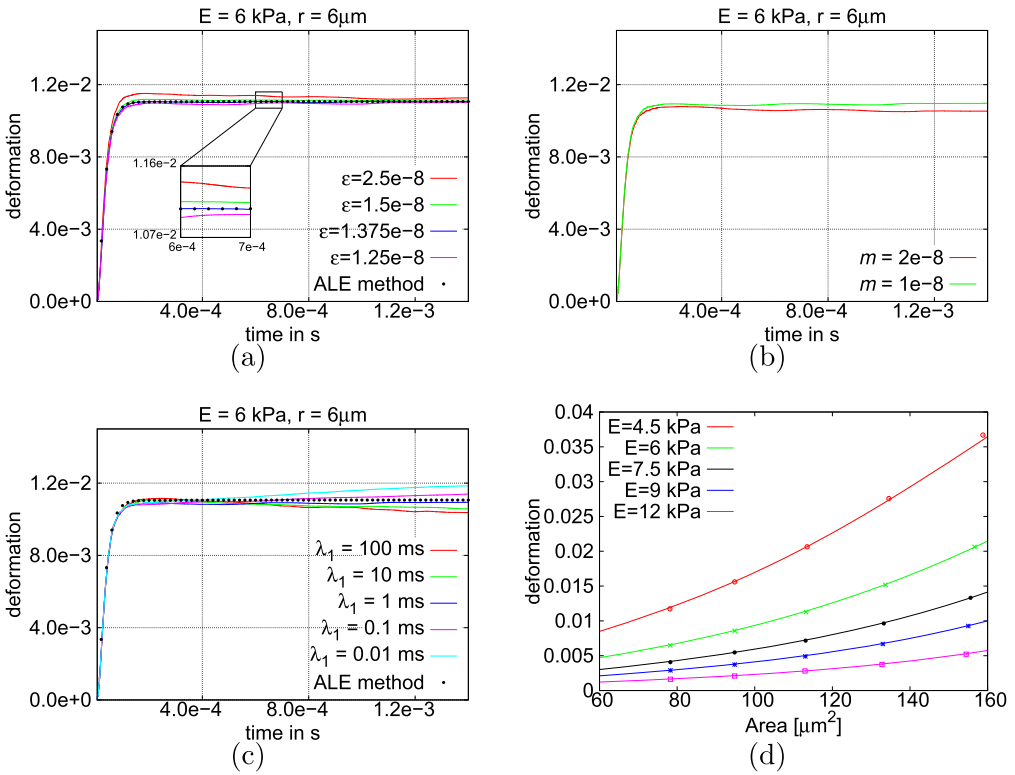

Fig. 3. Cell deformation in comparison to ALE reference values for varying parameters. In (a)–(c) we use the fixed physical parameters E = 6 kPa, $r = 6$ µm. The standard model parameters are $\lambda_1 = 1$ ms, $\epsilon = 1.25 \cdot 10^{-8}$ m and $m = 10^{-8}$ m^3 s/kg. One of these parameters is varied to investigate the influence of interface thickness ϵ (a), mobility m (b) and interfacial relaxation time λ_1 (c). (d) Provides stationary deformation values at $t = 1.4$ ms for different cell sizes and elastic moduli. Lines depict the results of the ALE method and marker points represent those of the phase-field method.

find already very good agreement to the ALE reference value. However for $\epsilon \to 0$ the deformation seems to converge to a value smaller than the reference solution. This is not surprising, as according Sec. 3, convergence to the sharp interface limit is only achieved when the constant mobility is decreased proportional to ϵ. Note, that the mobility controls the intrinsic Cahn–Hilliard dynamics that aims to reduce the surface and therefore decreases deformation.

Accordingly, we test the sensitivity of our results with respect to changes in the mobility in Fig. 3(b). As expected, higher mobility leads to a decrease in the steady-state deformation. But the quantitative effect of the Cahn–Hilliard dynamics is relatively low, as the deformation curve changes only slightly when the mobility is doubled.

Next, we vary the only free parameter in the Oldroyd-B equation, λ_1. We find that small variations of λ_1 have almost no influence on the evolution and steady state of the cell shape. To push our model to its limits, we vary λ_1 across several orders of magnitude in Fig. 3(c). We find that for very small λ_1, the cell deformation continuously increases and reaches no stationary state. In this case, the very small value of λ_1 leads to a very small relaxation time in the diffuse interface region and hence to a large dissipation of elastic stress there. The drop in elastic stress lets the cell increasingly deform. On the other hand, when λ_1 is very large, a small amount of elastic stress from the diffuse interface may accumulate in the fluid, leading to increased stiffening of the fluid and a decrease in cell deformation. We conclude that the parameter λ_1 has to be carefully chosen with a good choice being in the range of the problem's characteristic time scale.

Finally, we show that the results of the phase-field method are accurate over a range of cell sizes and elastic moduli. We simulated cells of five different sizes in the range ≈77 µm^2 to 160 µm^2. For each cell size, we chose five different values for the Young's Modulus between 4.5 kPa and 12 kPa. As seen in Fig. 3(d), the stationary deformation values of the phase-field method are in excellent agreement to the ALE reference values.

5. Illustration of the method's potential

In this section we perform further simulation studies in order to illustrate the potential of the presented phase-field FSI model. At first, we stick to the simulations of a cell in a cylindrical channel, but we now include surface tension to demonstrate the model's capability to simulate elastic bodies with strong surface tension, as they are common in biological applications. Therefore, we choose three different values for the surface tension, $\gamma = 5\text{e}{-4}$ N/m, $\gamma = 1\text{e}{-3}$ N/m and $\gamma = 5\text{e}{-3}$ N/m. Further parameters are E = 3 kPa and $r = 6$ µm. Fig. 4 shows that the surface tension has a strong influence on the stationary cell shape, which varies from triangular ($\gamma = 5\text{e}{-4}$ N/m) to almost circular ($\gamma = 5\text{e}{-3}$ N/m). The stiff surface

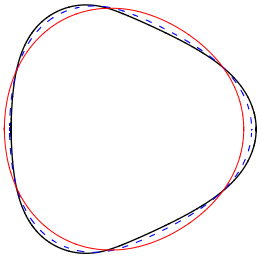

Fig. 4. Comparison of the steady state shapes for varying the surface tension $\gamma = 5e{-}4\,\mathrm{N/m}$ (black), $\gamma = 1e{-}3\,\mathrm{N/m}$ (blue dashed) $\gamma = 5e{-}3\,\mathrm{N/m}$ (thin red).

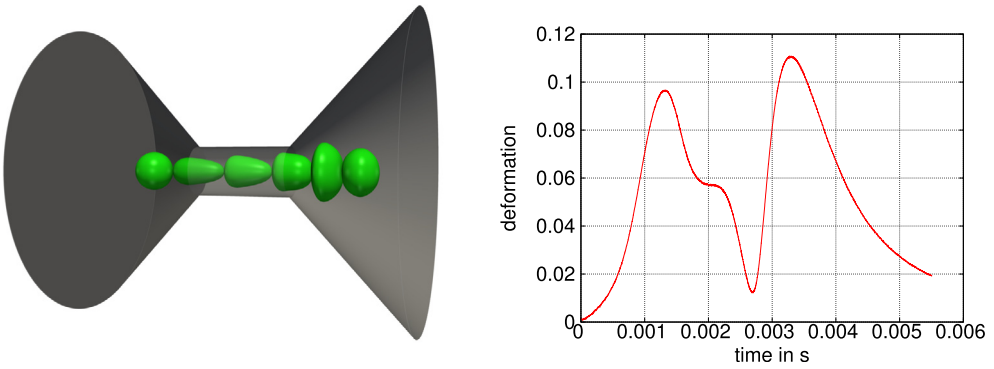

Fig. 5. Simulation of cell inflow/outflow in a modified channel geometry. The length of the narrow cylindrical channel is 40 µm. Left: Snapshots of cell shapes at $t = 0$ ms, 1.25 ms, 1.927 ms, 2.595 ms, 3.6 ms, 5.509 ms. Right: Cell deformation over time.

tension forces here are treated with a monolithic coupling of the interface advection and flow equations which relaxes any related time step restrictions [4, Sec. 4.1].

Next, we simulate the inflow and outflow of the cell. Such simulations are of great interest for biotechnological applications as the dynamics of cell deformation provides additional information on the cell's state. Therefore, we choose a realistic computation channel domain with a conical inlet/outlet of 45° [26]. The chosen parameter set is: $\mathrm{E} = 1.5\,\mathrm{kPa}$, $\gamma = 1e{-}3$ N/m, $\lambda = 1$ ms, $m = 10^{-8}$ m^3 s/kg, cell radius $r = 8$ µm and $\epsilon = 0.1$ µm. As for the cylindrical domain, a pressure difference is implemented between the left and the right boundary, which induces the flow. Fig. 5 shows a cut through the computational domain, the initial cell position and various cell shapes during the traversal of the channel.

The deformation curve in Fig. 5 shows a strong increase of cell deformation (elongation) during inflow, followed by a drop in deformation as soon as the cell is completely within the cylindrical part of the channel. The elongated cell almost approaches a stationary shape around $t = 2$ ms, but as it is already close to the outlet, the stationary state is never reached. Instead the cell starts to become shorter and wider. This leads to a drop in the deformation, followed by a peak when the cell reaches a maximum thickness and an oblate shape as it leaves the cylindrical channel. Afterwards, the cell relaxes back to a sphere.

Note, that such simulations are typically challenging for ALE methods as re-triangulations and interpolations are needed to reconnect the different grids while they move past each other. Our phase-field model needs neither re-triangulations nor interpolations to simulate this test case.

Finally, we illustrate the capability of the phase-field method to deal with contact between an elastic material and a rigid wall. Therefore we simulate a bouncing elastic ball immersed in a fluid. The fluid fills a cylindrical column of height 40 µm and radius 10 µm. The ball of radius $r = 6$ µm is initially placed in the middle of the column. The parameters for this toy problem are $\nu_1 = 4$ µPa · s, $\nu_{-1} = 10$ µPa · s, $E = 500$ Pa, $\rho_1 = 1000$ kg/m^3, $\rho_{-1} = 100$ kg/m^3, $\lambda_1 = 1$ ms, $\epsilon = 0.2$ µm, $m = 2 \cdot 10^{-9}$ m^3 s/kg.

A gravity force of magnitude 10^3 m/s$^2 \rho(\phi)$ is included to make the ball fall down. A no slip condition $\mathbf{v} = 0$ is specified at the top and bottom boundary of the liquid column. An additional no-wetting condition, $\phi = -1$, on all domain boundaries ensures that the ball is repelled from the boundaries. A free slip condition is imposed at the sides of the column.

Snapshots of the simulation results are shown in Fig. 6. The ball and the fluid around it are accelerated as the ball starts falling in the beginning of the simulation. Around $t = 0.18$ ms the ball 'touches' the rigid wall whereupon it is compressed in the direction of motion. After the maximum compression is reached around $t = 0.2$ ms the stored elastic energy is transformed into kinematic energy and the ball starts jumping upwards. This bouncing up and down is repeated several times, but quickly damped due to the viscosity of the surrounding fluid, such that the ball assumes a resting position 'lying' on the rigid wall.

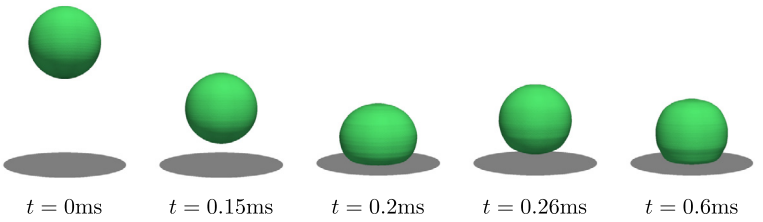

Fig. 6. Simulation snapshots of an elastic ball bouncing off a rigid wall at different times.

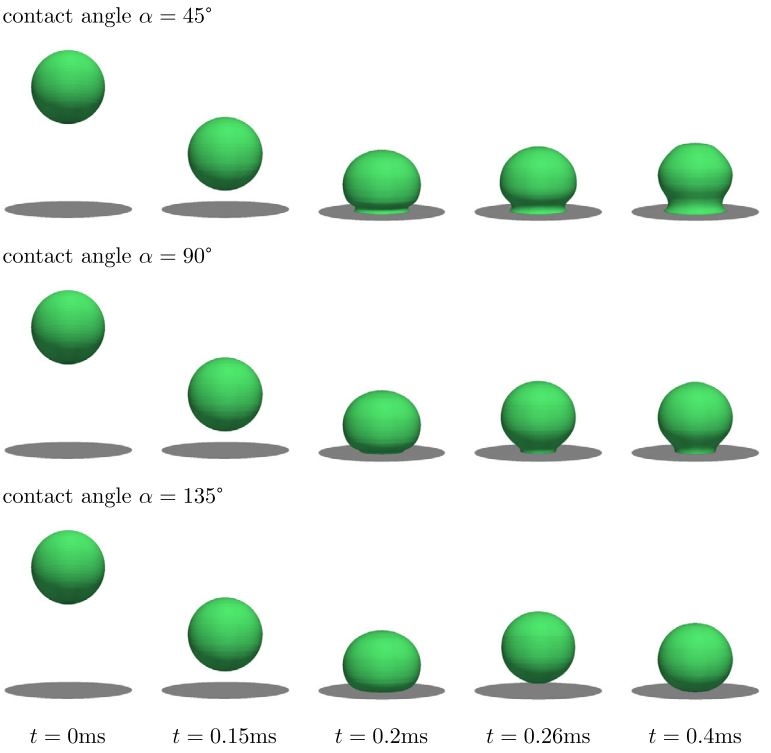

Fig. 7. Simulation snapshots of an adhesive elastic ball bumping into a rigid wall. The adhesive properties are determined by the involved surface energies through the contact angle α (see text).

Note, that no special treatment is needed to realize the contact dynamics here. The only thing is the no-wetting condition, $\phi = -1$, which needs to be imposed at the contact boundary.

In a last step, we extend the simulation even further by adding adhesion of the ball to the substrate (wall). Adhesive behavior is not only typical for fluids but also for some solid objects, like biological cells. Adhesion appears as soon as the surface tension γ_{ws} between the wall and the solid object is lower than the fluid/solid surface tension γ. According to the Young–Laplace law the balance of surface energies leads to the contact angle α with $\cos\alpha = (\gamma_{wf} - \gamma_{ws})/\gamma$, where γ_{wf} is the wall/fluid surface tension. The contact angle can be included by the Neumann boundary condition $\mathbf{n} \cdot \nabla\phi = \cos\alpha \cdot (1 - \phi^2)/(\sqrt{2}\epsilon)$, which can be derived by adding a wall potential to the system energy, see [7,2].

We repeat the simulation of the bouncing ball now with this new boundary condition to model adhesion. The parameters are as before, except for the mobility which is increased by a factor of 40 to overcome the typical stress singularity at the contact line, see [7] for a discussion. Fig. 7 shows the corresponding time evolution for three contact angles. For the smaller contact angles ($\alpha = 45°$, $90°$) the ball starts to adhere immediately after the first contact with the wall. Still, the ball is compressed shortly after contact and the elastic energy is released by lifting the ball up. But this time the ball remains bound to the wall and the oscillations are even more quickly damped. The ball develops an almost stationary position around $t = 0.4$ ms. In case of the larger contact angle, $\alpha = 135°$, the adhesion is too weak to keep the ball at the wall after first contact, which leads to the same bouncing as previously observed for the no-contact case. To our knowledge our method is the first numerical method to model adhesive elastic structures of arbitrary surface energy and contact angles in flow.

6. Conclusion

In this paper, we presented a novel phase-field model for fluid–structure-interaction. The model is based on a monolithic Navier–Stokes equation that solves for the velocity field in both, the fluid and the elastic domain. Viscous and elastic stresses are restricted to the corresponding domains by multiplication with their characteristic functions. To obtain the elastic stress, an additional Oldroyd-B – like equation is solved including an interfacial relaxation time. To close the system of equations, we derived globally thermodynamically consistent forces and fluxes using energy variation arguments. Provided that suitable power series expansions exist, matched asymptotic analysis shows the convergence of the derived equations to the traditional sharp interface formulation of FSI equations.

We conducted several numerical tests to validate the applicability and accuracy of the new model. A challenging benchmark scenario of an elastic cell traversing a fluid channel was employed and results are compared to reference values from ALE simulations [25]. We found very good agreement for various cell sizes and elastic moduli. In particular, we showed that the interface thickness ϵ and the mobility γ are small enough to influence the results only marginally. Results were also shown to be robust with respect to the introduced interfacial relaxation time.

Finally, we highlighted some distinct advantages of the new model as compared to traditional ALE approaches for FSI. We demonstrated the movement of a solid object through a fluidic channel without grid re-triangulations. We included strong surface energy, i.e. surface tension forces, into the model, whose stable discretization is one of the advantages of phase-field models. At last, we showed how easy it is to include contact dynamics into the model by simulating a ball bouncing off a wall. We concluded with the simulation of adhesion of an elastic ball to a rigid wall, a scenario which, to our knowledge, cannot be simulated with any other FSI model so far.

While we have restricted simulations to fluid–structure interaction, the model is capable to simulate any combination of viscous fluids, visco-elastic fluids and elastic solids. We therefore believe that the proposed phase-field model is well suited to tackle a range of complicated multi-physics problems, in particular from biology, in the future.

Acknowledgements

SA acknowledges support from the German Research Foundation (grant AL 1705/3) and support from the Saxon Ministry for Science and Art (SMWK MatEnUm-2).

Appendix A

A.1. Energy time derivative

In the following we present the complete computation of the time evolution of the energy given in Section 2.3. As discussed in [11], we assume $\sigma \in \mathbb{R}^{n\times n}$ to be a symmetric positive definite matrix (see [20] for a proof of this property) and thus calculate the trace of the matrix logarithm $\ln\sigma$ by

$$\operatorname{tr}(\ln\sigma) = \sum_{i=1}^{n} \ln\lambda_i \tag{A.1}$$

with the eigenvalues λ_i. According to Eq. (2.12), we consider three parts of the total energy:

$$E = \int_\Omega \underbrace{\frac{\rho(\phi)}{2}|\mathbf{v}|^2}_{\text{kinetic energy } E_{\text{kin}}} + \underbrace{\frac{\mu(\phi)}{2}\operatorname{tr}(\boldsymbol{\sigma} - \ln\boldsymbol{\sigma} - \mathbb{I})}_{\text{elastic energy } E_{\text{el}}} + \underbrace{\tilde{\gamma}\left(\frac{\epsilon}{2}|\nabla\phi|^2 + \frac{1}{\epsilon}W(\phi)\right)}_{\text{Cahn–Hilliard energy } E_{\text{CH}}} \mathrm{d}x\,. \tag{A.2}$$

The following identities will be useful to compute the time derivative of the three energies:

$$\nabla\mathbf{v} : \left(\nabla\mathbf{v} + \nabla\mathbf{v}^T\right) = \frac{1}{2}\left|\nabla\mathbf{v} + \nabla\mathbf{v}^T\right|^2 \tag{A.3}$$

$$\partial^\bullet\rho(\phi) = \rho'(\phi)\partial^\bullet\phi \tag{A.4}$$

$$\begin{aligned}\partial^\bullet\left(\frac{\rho(\phi)}{2}|\mathbf{v}|^2\right) &= \frac{1}{2}\partial^\bullet(\rho(\phi))|\mathbf{v}|^2 + \partial^\bullet(\mathbf{v})\cdot\rho(\phi)\mathbf{v} \\ &= \partial^\bullet(\rho(\phi)\mathbf{v})\cdot\mathbf{v} - \partial^\bullet\rho(\phi)\frac{|\mathbf{v}|^2}{2}\end{aligned} \tag{A.5}$$

In the following computation of the energy time derivatives, we will neglect boundary integrals that arise from integration by parts, as we assume appropriate boundary conditions. We further assume a closed system, i.e. the domain Ω moves with the flow field, which holds in particular if $\mathbf{v}\cdot\mathbf{n} = 0$ at the outer boundary $\partial\Omega$. This assumption simplifies our calculations since material derivatives will appear under the integral. Hence, we compute

$$\begin{aligned}
\frac{d}{dt}E_{\text{kin}} &\underset{(A.5)}{=} \int_\Omega \partial^\bullet(\rho(\phi)\mathbf{v})\mathbf{v} - \partial^\bullet\frac{\rho(\phi)}{2}|\mathbf{v}|^2\,\mathrm{d}x \\
&\underset{(2.8)}{=} \int_\Omega \left(\mathbf{F} + \nabla\cdot\left(\nu(\phi)\left(\nabla\mathbf{v}+\nabla\mathbf{v}^{\mathrm{T}}\right)\right) - \nabla p + \nabla\cdot(\mu(\phi)\sigma)\right)\cdot\mathbf{v} - \partial^\bullet\frac{\rho(\phi)}{2}|\mathbf{v}|^2\,\mathrm{d}x \\
&= \int_\Omega \mathbf{F}\cdot\mathbf{v} - \nu(\phi)\left(\nabla\mathbf{v}+\nabla\mathbf{v}^{\mathrm{T}}\right):\nabla\mathbf{v} + p\nabla\cdot\mathbf{v} - \mu(\phi)\sigma:\nabla\mathbf{v} - \partial^\bullet\frac{\rho(\phi)}{2}|\mathbf{v}|^2\,\mathrm{d}x \\
&\underset{(2.7)-(A.4)}{=} \int_\Omega -\frac{\nu(\phi)}{2}\left|\nabla\mathbf{v}+\nabla\mathbf{v}^{\mathrm{T}}\right|^2 - \mu(\phi)\sigma:\nabla\mathbf{v} + \mathbf{v}\cdot\mathbf{F} + \frac{\rho'(\phi)}{2}|\mathbf{v}|^2\nabla\cdot\mathbf{J}\,\mathrm{d}x,
\end{aligned}$$

where we have assumed either no flow across the boundaries, $\mathbf{v}_{|\partial\Omega}=0$, or no force, i.e. $\left(\nu(\phi)\left(\nabla\mathbf{v}+\nabla\mathbf{v}^{\mathrm{T}}\right) - pI + \mu(\phi)\sigma\right)\cdot\mathbf{n}=0$. We further compute

$$\begin{aligned}
\frac{d}{dt}E_{\text{CH}} &= \int_\Omega \tilde{\gamma}\partial^\bullet\left(\frac{\epsilon}{2}|\nabla\phi|^2 + \frac{1}{\epsilon}W(\phi)\right)\,\mathrm{d}x \\
&= \int_\Omega \tilde{\gamma}\left(\epsilon\nabla\phi\cdot\nabla\partial^\bullet\phi - \epsilon\nabla\phi\cdot\nabla\mathbf{v}\cdot\nabla\phi + \frac{1}{\epsilon}W'(\phi)\partial^\bullet\phi\right)\,\mathrm{d}x \\
&= \int_\Omega \tilde{\gamma}\left(-\epsilon\Delta\phi + \frac{1}{\epsilon}W'(\phi)\right)\partial^\bullet\phi + \mathbf{v}\cdot\left(\nabla\cdot\left(\epsilon\tilde{\gamma}\nabla\phi\otimes\nabla\phi\right)\right)\,\mathrm{d}x \\
&\underset{(2.7)}{=} \int_\Omega -\frac{\delta E_{\text{CH}}}{\delta\phi}\nabla\cdot\mathbf{J} + \mathbf{v}\cdot\left(\nabla\cdot\left(\epsilon\tilde{\gamma}\nabla\phi\otimes\nabla\phi\right)\right)\,\mathrm{d}x,
\end{aligned}$$

where we defined $\frac{\delta E_{\text{CH}}}{\delta\phi} := \tilde{\gamma}\left(-\epsilon\Delta\phi + \frac{1}{\epsilon}W'(\phi)\right)$. Note, that we have used the boundary condition $\mathbf{n}\cdot\nabla\phi = 0$ on $\partial\Omega$ here, which effectively leads to a contact angle of 90°, other contact angles can be treated by inclusion of a wall energy, see [7,2].

$$\begin{aligned}
\frac{d}{dt}E_{\text{el}} &= \int_\Omega \partial^\bullet\left(\frac{\mu(\phi)}{2}\right)\mathrm{tr}\left(\boldsymbol{\sigma} - \ln\boldsymbol{\sigma} - \mathbb{I}\right) + \frac{\mu(\phi)}{2}\partial^\bullet\,\mathrm{tr}\left(\boldsymbol{\sigma} - \ln\boldsymbol{\sigma} - \mathbb{I}\right)\,\mathrm{d}x \\
&\underset{(2.7),\,(A.4)}{=} \int_\Omega -\frac{\mu'(\phi)}{2}\nabla\cdot\mathbf{J}\,\mathrm{tr}\left(\boldsymbol{\sigma} - \ln\boldsymbol{\sigma} - \mathbb{I}\right) + \frac{\mu(\phi)}{2}\mathrm{tr}\left(\partial^\bullet\left(\sigma - \ln\sigma\right)\right)\,\mathrm{d}x \\
&= \int_\Omega -\frac{\mu'(\phi)}{2}\nabla\cdot\mathbf{J}\,\mathrm{tr}\left(\boldsymbol{\sigma} - \ln\boldsymbol{\sigma} - \mathbb{I}\right)\,\mathrm{d}x + \int_{\{\lambda=0\}}\frac{\mu(\phi)}{2}\mathrm{tr}\left((\mathbb{I}-\sigma^{-1})\partial^\bullet\sigma\right)\,\mathrm{d}x \\
&\quad + \int_{\Omega\setminus\{\lambda=0\}}\frac{\mu(\phi)}{2}\mathrm{tr}\left((\mathbb{I}-\sigma^{-1})\partial^\bullet\sigma\right)\,\mathrm{d}x \\
&\underset{(2.10)}{=} \int_\Omega -\frac{\mu'(\phi)}{2}\nabla\cdot\mathbf{J}\,\mathrm{tr}\left(\boldsymbol{\sigma} - \ln\boldsymbol{\sigma} - \mathbb{I}\right)\,\mathrm{d}x \\
&\quad + \int_{\Omega\setminus\{\lambda=0\}}\frac{\mu(\phi)}{2}\,\mathrm{tr}\left(\left(\mathbb{I}-\sigma^{-1}\right)\left(\nabla\mathbf{v}^T\cdot\sigma + \sigma\cdot\nabla\mathbf{v} - \frac{\alpha(\phi)}{\lambda(\phi)}\left(\sigma - \mathbb{I}\right)\right)\right)\,\mathrm{d}x.
\end{aligned}$$

Note, that Eq. (2.10) yields the boundedness of the last integrand in the set $\Omega\setminus\{\lambda=0\}$ given the solution is sufficiently smooth. Consequently, we obtain the variation of E as

$$\begin{aligned}
\mathrm{d}_t E = \int_\Omega & -\frac{\nu(\phi)}{2}\left|\nabla\mathbf{v}+\nabla\mathbf{v}^T\right|^2 - \mu(\phi)\sigma:\nabla\mathbf{v} + \mathbf{v}\cdot\mathbf{F} + \frac{\rho'(\phi)}{2}|\mathbf{v}|^2\nabla\cdot\mathbf{J} \\
& - \frac{\mu'(\phi)}{2}\nabla\cdot\mathbf{J}\,\mathrm{tr}\left(\sigma - \ln\sigma - \mathbb{I}\right) - \nabla\cdot\mathbf{J}\frac{\delta E_{\text{CH}}}{\delta\phi} + \mathbf{v}\cdot\left(\nabla\cdot\left(\epsilon\tilde{\gamma}\nabla\phi\otimes\nabla\phi\right)\right)\,\mathrm{d}x \\
& + \int_{\Omega\setminus\{\lambda=0\}}\frac{\mu(\phi)}{2}\,\mathrm{tr}\left(\left(\mathbb{I}-\sigma^{-1}\right)\left(\nabla\mathbf{v}^T\sigma + \sigma\nabla\mathbf{v} - \frac{\alpha(\phi)}{\lambda(\phi)}\left(\sigma - \mathbb{I}\right)\right)\right)\,\mathrm{d}x\,.
\end{aligned} \tag{A.6}$$

In order to reformulate the trace term in the last line, we use the symmetry of σ and the following properties:

$$\mathrm{tr}\left(ABA^{-1}\right) = \mathrm{tr}\,(B) \quad \text{for a regular matrix A} \tag{A.7}$$

$$\mathrm{tr}\,(AB) = A : B^T = A^T : B \tag{A.8}$$

$$\mathrm{tr}\,(\nabla \mathbf{v}) = \nabla \cdot \mathbf{v} = 0 \tag{A.9}$$

and thus get for $\lambda \neq 0$

$$\begin{aligned}
&\mathrm{tr}\left(\left(\mathbb{I} - \sigma^{-1}\right)\left(\nabla \mathbf{v}^T \sigma + \sigma \nabla \mathbf{v} - \frac{\alpha(\phi)}{\lambda(\phi)}\left(\sigma - \mathbb{I}\right)\right)\right) \\
&\underset{(A.7),\,(A.8)}{=} 2\sigma : \nabla \mathbf{v} - 2\mathrm{tr}\,(\nabla \mathbf{v}) - \frac{\alpha(\phi)}{\lambda(\phi)}\mathrm{tr}\left(\sigma + \sigma^{-1} - 2\mathbb{I}\right) \\
&\underset{(A.9)}{=} 2\sigma : \nabla \mathbf{v} - \frac{\alpha(\phi)}{\lambda(\phi)}\mathrm{tr}\left(\sigma + \sigma^{-1} - 2\mathbb{I}\right) .
\end{aligned} \tag{A.10}$$

Note, that also the last term of Eq. (A.10) is bounded, which follows from Eq. (2.10) and $|\mathrm{tr}(\sigma + \sigma^{-1} - 2I)| \leq C\|\sigma - I\|$ in a neighborhood of the identity matrix. We obtain a simplified version of Eq. (A.6):

$$\begin{aligned}
\mathrm{d}_t E = \int_\Omega & -\frac{\nu(\phi)}{2}\left|\nabla \mathbf{v} + \nabla \mathbf{v}^T\right|^2 + \mathbf{v} \cdot \mathbf{F} + \frac{\rho'(\phi)}{2}|\mathbf{v}|^2 \nabla \cdot \mathbf{J} - \nabla \cdot \mathbf{J}\frac{\delta E_{\mathrm{CH}}}{\delta \phi} \\
& - \frac{\mu'(\phi)}{2}\nabla \cdot \mathbf{J}\,\mathrm{tr}\,(\sigma - \ln \sigma - \mathbb{I}) + \mathbf{v} \cdot \left(\nabla \cdot (\epsilon \tilde{\gamma} \nabla \phi \otimes \nabla \phi)\right) \mathrm{d}x \\
& - \int_{\Omega \setminus \{\lambda = 0\}} \frac{\mu(\phi)\alpha(\phi)}{2\lambda(\phi)}\mathrm{tr}\left(\sigma + \sigma^{-1} - 2\mathbb{I}\right)\,\mathrm{d}x .
\end{aligned}$$

Furthermore we reformulate the density term in (A.6) applying integration by parts twice and using that $\rho'(\phi)$ is constant:

$$\int_\Omega \frac{\rho'(\phi)}{2}|\mathbf{v}|^2 \nabla \cdot \mathbf{J} = \int_\Omega -\rho'(\phi)\mathbf{v} \cdot (\nabla \mathbf{v} \cdot \mathbf{J}) = \int_\Omega \mathbf{v} \cdot \left(\nabla \cdot (\rho'(\phi)\mathbf{v} \otimes \mathbf{J})\right) \mathrm{d}x ,$$

which yields the energy time derivative given in Eq. (2.13).

A.2. Time-discrete axisymmetric equations

We consider axisymmetric flow and geometries which allows to rewrite the equations in a 2D manner using cylindrical coordinates. Thereby the 2D meridian domain $\Omega_{2D} = \{(x_0, r) |\ 0 \leq x_0 \leq a, 0 \leq r \leq b\}$ represents the 3D domain $\Omega = \{(x_0, x_1, x_2) |\ x_1 = r\cos(\theta), x_2 = r\sin(\theta), (x_0, r) \in \Omega_{2D}, \theta \in [0, 2\pi)\}$, see Fig. 8 for an illustration. In the following, all fields are defined on Ω_{2D}, the velocity field on this domain is defined to consist of only axial and radial component $\mathbf{v} = (v_0, v_r)$. The gradient, divergence and Laplace operator in the cylindrical coordinate system are defined by

$$\nabla = (\partial_{x_0}, \partial_r), \qquad \tilde{\nabla} \cdot = \left(\partial_{x_0}, \frac{1}{r} + \partial_r\right), \qquad \tilde{\Delta} = \tilde{\nabla} \cdot \nabla = \partial_{x_0 x_0} + \partial_{rr} + \frac{1}{r}\partial_r .$$

As derivatives in azimuthal (θ-) direction vanish, the strain tensor assumes the form

$$\sigma := \begin{pmatrix} \sigma_{00} & \sigma_{01} & 0 \\ \sigma_{10} & \sigma_{11} & 0 \\ 0 & 0 & \sigma_{\theta\theta} \end{pmatrix} .$$

For a shorter notation we introduce the matrices

$$\sigma_{2D} = \begin{pmatrix} \sigma_{00} & \sigma_{01} \\ \sigma_{10} & \sigma_{11} \end{pmatrix}, \qquad \mathbb{I}_{2D} = \begin{pmatrix} 1 & 0 \\ 0 & 1 \end{pmatrix}$$

We assume the density ρ to be constant. Hence, we may neglect the corresponding term in Eq. (2.14). The lower, upper, right, and left boundaries are denoted by Γ_1, Γ_2, Γ_3 and Γ_4, respectively. In the comparison study with the ALE simulations, the computational domain is moved along with the cell velocity, i.e., the spatially averaged velocity of the cell, named $\mathbf{v}_b$, is subtracted from the velocity in the advection terms in Eqs. (2.7), (2.8) and (2.10). This modification helps to reduce the amount of remeshing and also leads to a consistent comparison with the ALE model which also applied such a co-moving grid.

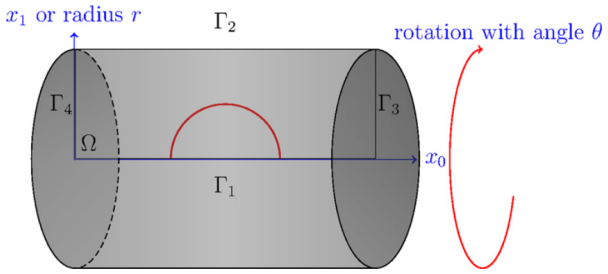

Fig. 8. Illustration of the axisymmetric computational domain. The boundary line segments Γ_1 to Γ_4 circumscribe the rectangular 2D domain Ω_{2D}. The use of axisymmetric terms in the governing system of equations, allows to simulate the flow of an initially spherical object through a cylinder.

For the time discretization we chose an equidistant time partitioning with time step size τ. Thereby we consider the discrete time derivative $d_t f^m := \frac{f^m - f^{m-1}}{\tau}$ for some scalar variable f and time step index m. At each time step we solve the following systems in Ω_{2D}:

1. The Navier–Stokes system

$$\begin{aligned}
&\rho\left(d_t\mathbf{v}^m + \left(\mathbf{v}^{m-1} - \mathbf{v}_b\right)\cdot\nabla\mathbf{v}^m\right) + \nabla p^m - \tilde{\nabla}\cdot\left(\nu^{m-1}\left(\nabla\mathbf{v} + \nabla\mathbf{v}^T\right)\right)\\
&= \frac{\nu^{m-1}}{r}\begin{pmatrix}0\\ -\frac{2}{r}v_1^m\end{pmatrix} + \tilde{\nabla}\cdot\left(\mu^{m-1}\left(\sigma_{2D}^{m-1} - \mathbb{I}_{2D}\right)\right) - (\sigma_{\theta\theta}^{m-1} - 1)\frac{\mu^{m-1}}{r}\begin{pmatrix}0\\1\end{pmatrix}\\
&\quad - \epsilon\tilde{\gamma}\tilde{\nabla}\cdot\left(\nabla\phi^m\otimes\nabla\phi^{m-1}\right) \qquad (A.11)\\
&\tilde{\nabla}\cdot\mathbf{v}^m = 0 \qquad (A.12)
\end{aligned}$$

where $\nu^m = \nu(\phi^m)$, $\mu^m = \mu(\phi^m)$. We apply the following boundary conditions for the velocity:

$$\begin{aligned}
\mathbf{v} &= 0 \qquad \text{on } \Gamma_2\,, \qquad (A.13)\\
v_1 &= 0 \qquad \text{on } \Gamma_1\,. \qquad (A.14)
\end{aligned}$$

Equation (A.13) corresponds to a no-slip condition at the channel wall and (A.14) avoids a radial flow at the symmetry axis. In case of channel flow, we set periodic boundary conditions for $\mathbf{v}$ on Γ_4 and Γ_3 and

$$\begin{aligned}
p &= 0 \qquad \text{on } \Gamma_3\,,\\
p &= p_0 \qquad \text{on } \Gamma_4\,,
\end{aligned}$$

where $p_0 > 0$ imposes the desired pressure difference between Γ_4 and Γ_3 driving the flow through the channel.

2. The Cahn–Hilliard system is split into two second order equations which are assembled together

$$\begin{aligned}
&d_t\phi^m + \left(\mathbf{v}^m - \mathbf{v}_b\right)\cdot\nabla\phi^{m-1} - \tilde{\nabla}\cdot\left(m(\phi^{m-1})\nabla q^m\right) = 0 \qquad (A.15)\\
&q^m + \epsilon\tilde{\Delta}\phi^m - \frac{1}{\epsilon}W'(\phi^m) = 0\,. \qquad (A.16)
\end{aligned}$$

To avoid the nonlinear terms, we choose a Taylor expansion of linear order for $W'(\phi^m)$:

$$\begin{aligned}
W'\left(\phi^m\right) &= \left(\phi^m\right)^3 - \phi^m\\
&\approx 3\left(\phi^{m-1}\right)^2\phi^m - 2\left(\phi^{m-1}\right)^3 - \phi^m. \qquad (A.17)
\end{aligned}$$

As for the velocity, periodic boundary conditions for ϕ and c are given on Γ_3 and Γ_4. No flux conditions are used on the other boundaries. Note, that the Navier–Stokes and Cahn–Hilliard system are fully coupled here, due to the appearance of ϕ^m in (A.11) and $\mathbf{v}^m$ in (A.15). Consequently the systems are assembled and solved monolithically. This coupling is adopted from [4, Sec. 4.1] and relaxes the stiffness of surface tension forces.

3. The Oldroyd-B system

$$\begin{aligned}
&\lambda(\phi^m)\left(d_t\sigma_{2D}^m + \left(\mathbf{v}^m - \mathbf{v}_b\right)\nabla\sigma_{2D}^m - \nabla\mathbf{v}^m\cdot\sigma_{2D}^{m-1} - \sigma_{2D}^{m-1}\cdot\left(\nabla\mathbf{v}^m\right)^T\right)\\
&\quad = D\left(\Delta\sigma_{2D}^m - \Delta\sigma_{2D}^{m-1}\right) - \alpha(\phi^m)\left(\sigma_{2D}^m - \mathbb{I}\right) \qquad (A.18)
\end{aligned}$$

$$\lambda(\phi^m)\left(d_t\sigma_{\theta\theta}^m + \left(\mathbf{v}^m - \mathbf{v}_b\right)\nabla\sigma_{\theta\theta}^m - 2\frac{v_1^m}{r}\sigma_{\theta\theta}^{m-1}\right)$$
$$= D\left(\Delta\sigma_{\theta\theta}^m - \Delta\sigma_{\theta\theta}^{m-1}\right) - \alpha(\phi^m)\left(\sigma_{\theta\theta}^m - \mathbb{I}\right). \tag{A.19}$$

Note that (A.18)–(A.19) express 5 equations for the 5 unknowns of the elastic stress tensor, one of which is redundant due to symmetry of σ_{2D}. To ensure numerical stability we have added a small artificial diffusion term with $D = 2 \cdot 10^{-10}$ m^2, whereupon natural no-flux boundary conditions emerge.

In practice we solve in every time steps for approximately 230, 000 degrees of freedom (in total for all solution variables). The computational costs on a single core amount to approximately 18 seconds per time step (including the time for remeshing) in case of the example in Fig. 3(a) with $\epsilon = 2.5\text{e}{-8}$ m. The duration of the complete simulation depends on the chosen time step size τ. In the mentioned case, we chose $\tau = 5\text{e}{-7}$ seconds and obtain a duration of around 14 hours.

References

[1] H. Abels, H. Garcke, G. Grün, Thermodynamically consistent, frame indifferent diffuse interface models for incompressible two-phase flows with different densities, Math. Models Methods Appl. Sci. 22 (03) (2012) 1150013.
[2] S. Aland, Phase field models for two-phase flow with surfactants and biomembranes, in: Transport Processes at Fluidic Interfaces, Springer, 2017, pp. 271–290.
[3] S. Aland, Modelling of Two-Phase Flow with Surface Active Particles, PhD Thesis, TU Dresden, 2012.
[4] S. Aland, Time integration for diffuse interface models for two-phase flow, J. Comput. Phys. 262 (2014) 58–71.
[5] S. Aland, F. Chen, An efficient and energy stable scheme for a phase-field model for the moving contact line problem, Int. J. Numer. Methods Fluids 81 (11) (2016) 657–671.
[6] S. Aland, S. Egerer, J. Lowengrub, A. Voigt, Diffuse interface models of locally inextensible vesicles in a viscous fluid, J. Comput. Phys. 277 (2014) 32–47.
[7] S. Aland, J. Lowengrub, A. Voigt, Two-phase flow in complex geometries: a diffuse domain approach, Comput. Model. Eng. Sci. 57 (1) (2010) 77–106.
[8] S. Aland, J. Lowengrub, A. Voigt, A continuum model of colloid-stabilized interfaces, Phys. Fluids 23 (6) (2011) 062103.
[9] S. Aland, A. Voigt, Benchmark computations of diffuse interface models for two-dimensional bubble dynamics, Int. J. Numer. Methods Fluids 69 (3) (2012) 747–761.
[10] J. Bonet, R.D. Wood, Nonlinear Continuum Mechanics for Finite Element Analysis, Cambridge University Press, 1997.
[11] S. Boyaval, T. Lelièvre, C. Mangoubi, Free-energy-dissipative schemes for the Oldroyd-B model, ESAIM: M2AN 43 (3) (2009) 523–561.
[12] G. Cottet, E. Maitre, T. Milcent, Eulerian formulation and level set models for incompressible fluid–structure interaction, ESAIM: M2AN 42 (3) (2008) 471–492.
[13] S. Frei, T. Richter, T. Wick, Eulerian techniques for fluid–structure interactions: part I – modeling and simulation, in: Numerical Mathematics and Advanced Applications, ENUMATH 2013, Springer, 2015, pp. 745–753.
[14] G. Grün, F. Klingbeil, Two-phase flow with mass density contrast: stable schemes for a thermodynamic consistent and frame-indifferent diffuse-interface model, J. Comput. Phys. 257 (2014) 708–725.
[15] H. Garcke, K. Lam, B. Stinner, Diffuse interface modelling of soluble surfactants in two-phase flow, Commun. Math. Sci. 12 (8) (2014) 1475–1522.
[16] P. He, R. Qiao, A full-Eulerian solid level set method for simulation of fluid–structure interactions, Microfluid. Nanofluid. 11 (5) (2011) 557.
[17] C. Hirt, B. Nichols, Volume of fluid method for the dynamics of free boundaries, J. Comput. Phys. 39 (1) (1981) 201–225.
[18] G. Hou, J. Wang, A. Layton, Numerical methods for fluid–structure interaction – a review, Commun. Comput. Phys. 12 (2) (2012) 337–377.
[19] T.J. Hughes, W.K. Liu, T.K. Zimmermann, Lagrangian–Eulerian finite element formulation for incompressible viscous flows, Comput. Methods Appl. Mech. Eng. 29 (3) (1981) 329–349.
[20] M.A. Hulsen, A sufficient condition for a positive definite configuration tensor in differential models, J. Non-Newton. Fluid Mech. 38 (1) (1990) 93–100.
[21] T. Krüger, M. Gross, D. Raabe, F. Varnik, Crossover from tumbling to tank-treading-like motion in dense simulated suspensions of red blood cells, Soft Matter 9 (37) (2013) 9008–9015.
[22] A. Legay, J. Chessa, T. Belytschko, An Eulerian–Lagrangian method for fluid–structure interaction based on level sets, Comput. Methods Appl. Mech. Eng. 195 (17) (2006) 2070–2087.
[23] X. Li, J. Lowengrub, A. Rätz, A. Voigt, Solving PDEs in complex geometries: a diffuse domain approach, Commun. Math. Sci. 7 (1) (2009) 81.
[24] J. Lowengrub, J. Allard, S. Aland, Numerical simulation of endocytosis: viscous flow driven by membranes with non-uniformly distributed curvature-inducing molecules, J. Comput. Phys. 309 (2016) 112–128.
[25] M. Mokbel, D. Mokbel, A. Mietke, N. Träber, S. Girardo, O. Otto, J. Guck, S. Aland, Numerical simulation of real-time deformability cytometry to extract cell mechanical properties, ACS Biomater. Sci. Eng. 3 (11) (2017) 2962–2973.
[26] O. Otto, P. Rosendahl, A. Mietke, S. Golfier, C. Herold, D. Klaue, S. Girardo, S. Pagliara, A. Ekpenyong, A. Jacobi, M. Wobus, N. Töpfner, U. Keyser, J. Mansfeld, E. Fischer-Friedrich, J. Guck, Real-time deformability cytometry: on-the-fly cell mechanical phenotyping, Nat. Methods 12 (3) (2015) 199.
[27] J. Sethian, Level Set Methods and Fast Marching Methods Evolving Interfaces in Computational Geometry, Fluid Mechanics, Computer Vision, and Materials Science, Cambridge University Press, 1999.
[28] K. Sugiyama, S. Ii, S. Takeuchi, S. Takagi, Y. Matsumoto, A full Eulerian finite difference approach for solving fluid–structure coupling problems, J. Comput. Phys. 230 (3) (2011) 596–627.
[29] P. Sun, J. Xu, L. Zhang, Full Eulerian finite element method of a phase field model for fluid–structure interaction problem, Comput. Fluids 90 (2014) 1–8.
[30] G. Tierra, J.P. Pavissich, R. Nerenberg, Z. Xu, M.S. Alber, Multicomponent model of deformation and detachment of a biofilm under fluid flow, J. R. Soc. Interface 12 (106) (2015) 20150045.
[31] S. Turek, J. Hron, Proposal for numerical benchmarking of fluid–structure interaction between an elastic object and laminar incompressible flow, in: Fluid–Structure Interaction: Modelling, Simulation, Optimisation, Springer, Berlin, Heidelberg, 2006, pp. 371–385.
[32] S. Vey, A. Voigt, AMDiS: adaptive multidimensional simulations, Comput. Vis. Sci. 10 (1) (2007) 57–67.
[33] T. Witkowski, S. Ling, S. Praetorius, A. Voigt, Software concepts and numerical algorithms for a scalable adaptive parallel finite element method, Adv. Comput. Math. 41 (6) (2015) 1145–1177.